Chinese Chemical Letters 35 (2024) 109245

Contents lists available at ScienceDirect

Chinese Chemical Letters

journal homepage: www.elsevier.com/locate/cclet

Construction of Z-scheme Cu-CeO_2/BiOBr heterojunction for enhanced photocatalytic degradation of sulfathiazole

Xingmin Chen[a,1], Yunyun Wu[b,1], Yao Tang[b], Peishen Li[c], Shuai Gao[b], Qiang Wang[b,*], Wen Liu[c], Sihui Zhan[a,*]

[a] College of Environmental Sciences and Engineering, Nankai University, Tianjin 300350, China
[b] Laboratory for Micro-Sized Functional Materials & College of Elementary Education and Department of Chemistry, Capital Normal University, Beijing 100048, China
[c] College of Environmental Sciences and Engineering, The Key Laboratory of Water and Sediment Sciences (MOE), Peking University, Beijing 100871, China

ARTICLE INFO

Article history:
Received 13 June 2023
Revised 7 October 2023
Accepted 25 October 2023
Available online 29 October 2023

Keywords:
Cu-CeO_2/BiOBr nanoheterojunction
Photocatalytic degradation
Sulfathiazole
Z-scheme

ABSTRACT

The utilization of an efficient photocatalyst is crucial for the photocatalytic degradation of antibiotics in water through visible light, which is an imperative requirement for the remediation of water environments. In this study, a novel Cu-CeO_2/BiOBr Z-type heterojunction was synthesized by calcination and hydrothermal methods, and the degradation rate of sulfathiazole (STZ) antibiotic solution was studied using simulated illumination (300 W xenon lamp). The results indicated that 3% Cu-CeO_2/BiOBr achieved a degradation rate of 92.3% within 90 min when treating 20 mg/L STZ solution, demonstrating its potential for practical water treatment applications. Characterization using various chemical instruments revealed that 3% Cu-CeO_2/BiOBr exhibited the lowest electron-hole recombination rate and electron transfer resistance. Furthermore, the utilization of ESR data and quenching experiments has substantiated the involvement of hydroxyl radicals ($^{\bullet}OH$) and superoxide radicals ($^{\bullet}O_2^-$) as the primary active species. Consequently, a plausible degradation mechanism has been inferred. These findings offer a prospective approach for the development of heterojunction materials with appropriate band matching.

Sulfathiazole (STZ) is an essential sulfonamide antibiotic utilized in the treatment and prevention of prevalent human and livestock ailments, rendering it an indispensable component of medical therapeutics [1,2]. However, a limited proportion of antibiotics demonstrate *in vivo* efficacy, with the majority being excreted into the external environment *via* urine or feces, and subsequently detected in diverse environmental matrices as mother or metabolite. These residues have the potential to foster the development of drug-resistant genes or bacteria, thereby posing a potential threat to aquatic organisms and human health [3]. Consequently, the development of cost-effective and efficient water treatment technologies for the removal of STZ from water is of utmost importance. Currently, the primary methods for eliminating sulfonamides from water involve a combination of physical, chemical, and biological treatment approaches. However, STZ cannot be completely removed from water by conventional methods due to its stable structure, high mobility and low biodegradability and long-term resistance [4–6]. Therefore, there is a growing interest in risk-free methods for the treatment of residual sulfanilamide antibiotics.

In recent years, semiconductor photocatalytic technology has gained popularity due to its high removal efficiency, use of sunlight, and strong redox ability [7]. Designing a catalyst with excellent photocatalytic activity and stability is crucial for the successful application of photocatalytic technology. BiOBr has gained popularity among researchers as a semiconductor material for photocatalytic degradation due to its unique layered structure, adjustable band gap, and ease of modification [8]. However, single BiOBr is not sufficient to meet actual production needs in the long run due to the rapid recombination rate of photogenerated e^-/h^+ pairs and low visible light response efficiency [9]. To improve the limitations of single BiOBr, one of the most effective strategies is to form heterojunction structures by combining different semiconductors. This minimizes the recombination of light-generated e^-/h^+ pairs and enhances the absorption capacity of visible light, thereby improving the redox capacity of photocatalytic degradation. The construction of Z-type heterojunction is one of the most effective ways to improve the photocatalytic activity. For example, Niu *et al.* [10] synthesized g-C_3N_4@Bi/BiOBr Z-type heterojunction by mi-

* Corresponding authors.
E-mail addresses: qwchem@gmail.com (Q. Wang), sihuizhan@nankai.edu.cn (S. Zhan).
[1] These authors contributed equally to this work.

https://doi.org/10.1016/j.cclet.2023.109245
1001-8417/

crowave solvothermal method, which greatly improved the degradation rate of ciprofloxacin. Xie *et al.* [11] constructed a Z-type carrier migration system by uniformly loading carbonized polymer points on BiOBr nanosheets through a low-thermal solid-state chemical reaction, which greatly improved its reduction rate of CO_2. Liu *et al.* [12] successfully synthesized direct Z-type BiOBr/CuI heterostructures using a simple solvothermal method, with a phenol removal rate of 98.4% within 150 min. Gao *et al.* [13] used the solvent heat method to prepare a Z-type g-C_3N_4@PDA/BiOBr heterojunction nanomaterial that exhibited high degradation activity for sulfamethoxazole. Optimized photocatalysts have great potential for future green and solar-driven synthesis and removal of refractory organic pollutants from real water bodies.

The rare earth oxide CeO_2 has garnered significant interest in various fields, including photocatalysis, dye cells, oxygen storage devices, and biomedicine [14]. CeO_2 is a photocatalyst material that is environmentally benign and typically exhibits noteworthy photocatalytic activity when exposed to ultraviolet radiation, owing to its proficient oxygen transport capability, abundant oxygen vacancies, and resistance to photodegradation [14–16]. Despite being a wide-band semiconductor (2.8–3.1 eV), CeO_2 exhibits a low utilization rate of visible light, thereby limiting its potential application in the field of photocatalysis [17,18]. To improve the material's performance under visible light, researchers have made numerous efforts such as changing the crystal lattice structure through element doping (*e.g.*, Cu, Co, Yb, Fe, Pb, N, and La) and narrowing the band gap to enhance its photocatalytic activity [19,20]. Shahzadi *et al.* successfully doped La into CeO_2 quantum dots by hydrothermal method, and found that CeO_2 doped with 6% La showed significant antibacterial activity against *Escherichia coli* at a higher concentration, and showed significant methylene blue catalytic degradation performance in alkaline media [21]. Cu doping exhibits significant interfacial redox activity among the elements, owing to the presence of Cu^{+}/Cu^{2+} and Ce^{3+}/Ce^{4+} ions [19]. Moreover, Cu is an essential trace element in the body, which is abundant and low-cost [22]. Mousavi-Kamazani *et al.* synthesized Cu-doped CeO_2 nanomaterials by a simple acoustochemical method. Cu reduced the band gap value of CeO_2, greatly improved the photocatalytic activity of doped CeO_2, and the degradation rate of methyl orange reached 99% in 45 min [19]. Therefore, Cu was used as a dopant of CeO_2 to prepare a visible photocatalyst with a narrower band gap.

Based on the above analysis, combining Cu-doped CeO_2 with BiOBr to form a heterojunction structure will enhance the transport and separation of photogenerated charge, expand the scope of visible light absorption, and enhance the photocatalytic ability [23,24]. This study introduces a range of Cu-CeO_2/BiOBr nanoheterogenesis photocatalysts, synthesized through uncomplicated calcination and solvothermal techniques, with varying Cu-CeO_2 ratios. The effectiveness of the catalysts was assessed through an analysis of the degradation of STZ, a representative pollutant, using photocatalysis. Results indicate that the removal rate of sulfathiazole by 3% Cu-CeO_2/BiOBr can reach 92.3% within 90 min of simulated solar irradiation. Furthermore, the effects of catalyst utilization, solution pH, and antibiotic concentration on STZ removal were thoroughly investigated, and the repeatability and stability of STZ degradation were evaluated. The possible degradation mechanism of STZ was established through quenching and ESR capture experiments.

Detailed information on chemical agents and instruments for the characterization of the material structure, material preparation, and photocatalytic degradation experiments are included in the supporting information.

The surface morphology and microstructure of the catalyst were analyzed by scanning electron microscopy (SEM), transmission electron microscopy (TEM), high-resolution transmission electron microscopy (HRTEM) and selected area electron diffraction (SAED). According to the SEM images (Figs. 1a–c), the Cu-CeO_2 compound predominantly manifests as nanoparticles, whereas the BiOBr structure exhibits a hydrangea-like morphology. This configuration facilitates the growth of Cu-CeO_2 nanoparticles onto the surface of the BiOBr flower ball, thereby engendering a heterojunction structure of Cu-CeO_2/BiOBr. The microstructure of the nanocomposite can be more clearly observed through the TEM image of 3% Cu-CeO_2/BiOBr (Fig. 1d). The connection between Cu-CeO_2 and BiOBr is conducive to the separation and transfer of electric charge, thus reducing the recombination rate of the photogenic e^{-}/h^{+} pair. Additionally, HRTEM images of 3% Cu-CeO_2/BiOBr (Fig. 1e) reveal lattice spacing of 0.312 nm and 0.282 nm for Cu-CeO_2 and BiOBr, respectively, corresponding to the (111) crystal plane of Cu-CeO_2 and the (102) crystal plane of BiOBr [25]. Furthermore, the SAED image in Fig. 1f confirms the existence and orientation of the material's crystal plane, consistent with the HRTEM results. The presence and homogeneous dispersion of copper, cerium, oxygen, bromine, and bismuth in 3% Cu-CeO_2/BiOBr heterojunction materials were verified through TEM-EDS elemental mapping analysis (Figs. 1g–m).

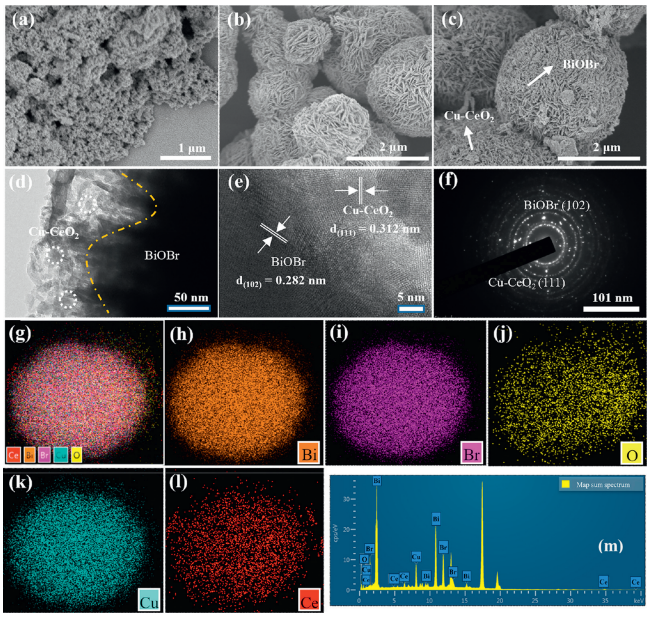

Fig. 1. SEM images of (a) Cu-CeO_2, (b) BiOBr and (c) Cu-CeO_2/BiOBr. (d) TEM, (e) HRTEM and (f) SAED images of 3% Cu-CeO_2/BiOBr. (g–m) TEM-EDS elemental mapping images of Bi, Br, O, Cu, and Ce, with panel (g) showing the combined distribution.

X-ray diffraction (XRD) analysis can determine the degree of purity and crystal phase composition of the synthesized samples. Fig. 2a shows that the Cu-CeO_2 sample shows all diffraction peaks of CeO_2, at $2\theta = 28.54$ °, 33.07 °, 47.43 ° and 56.32 ° corresponding to (111), (200), (220) and (311) crystal planes of CeO_2 respectively (JCPDS #43-1002); while the XRD spectrum of BiOBr mainly shows seven major peaks at 10.83°, 25.11°, 31.62°, 32.17°, 46.23°, 53.51° and 57.19°, which correspond to (001), (101), (102), (110), (112), (200), (211) and (212) crystal planes of BiOBr (JCPDS #09-0393) [26]. It is worth noting that the characteristic peaks in the 3% Cu-CeO_2/BiOBr sample exhibit a resemblance to those of BiOBr, which indicates that the Cu-CeO_2 coupling has no great impact on the crystal structure of BiOBr. The weak signal peak of Cu-CeO_2 may be attributed to the low content deposited on the surface of BiOBr and its high dispersion. This phenomenon has been previously reported in similar studies [27].

The FTIR analysis was conducted within the wavelength range of 400-4000 cm^{-1} to investigate the chemical bond vibration char-

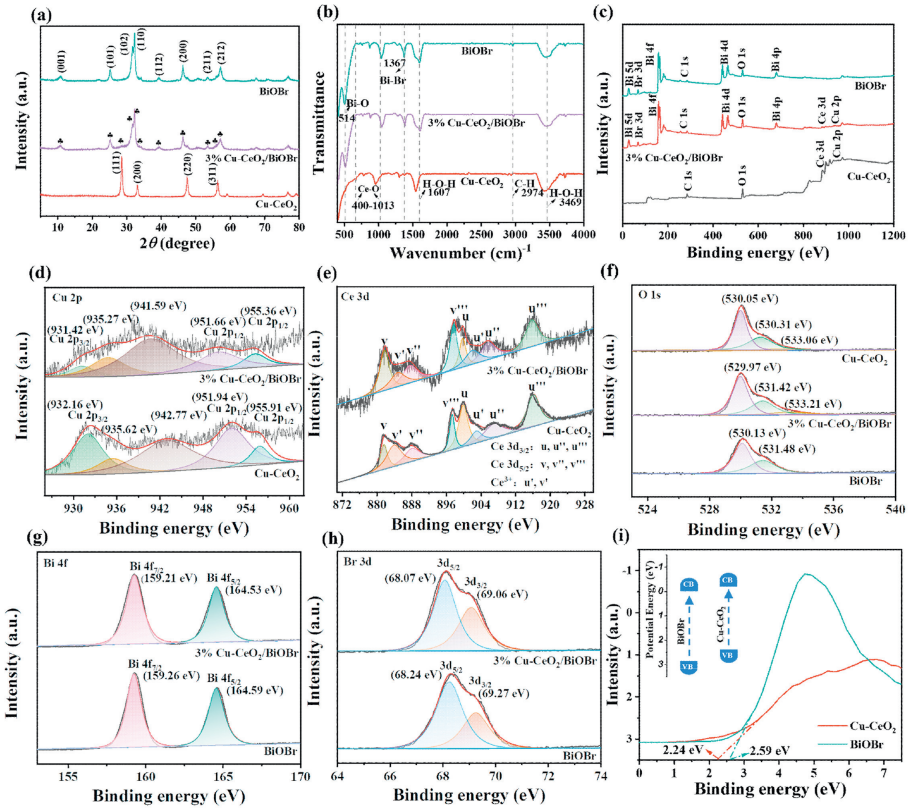

Fig. 2. (a) XRD, (b) FTIR and (c) XPS survey spectra of Cu-CeO_2, BiOBr and 3% Cu-CeO_2/BiOBr. (d) Cu 2p and (e) Ce 3d spectra of Cu-CeO_2 and 3% Cu-CeO_2/BiOBr. (f) O 1s spectra of Cu-CeO_2, BiOBr and 3% Cu-CeO_2/BiOBr. (g) Bi 4f and (h) Br 3d spectra of BiOBr and 3% Cu-CeO_2/BiOBr. (i) VB XPS spectra of Cu-CeO_2 and BiOBr.

acteristics of prepared Cu-CeO_2/BiOBr nanomaterials, thereby ensuring successful synthesis. Fig. 2b demonstrates that the asymmetric tensile vibration of the Ce-O bond accounts for the peaks observed at 400-1013 cm^{-1} for Cu-CeO_2 and 3% Cu-CeO_2/BiOBr [28], whereas the stretching vibration of the Bi-O bond and the asymmetric stretching of the Bi-Br bond pertain to the characteristic peaks at 514 cm^{-1} and 1376 cm^{-1} of BiOBr and 3% Cu-CeO_2/BiOBr [29]. The stretching vibration and bending vibration of the O-H bond of water molecules are the underlying causes of the two noticeable signal peaks, respectively, observed at 1607 cm^{-1} and 3469 cm^{-1} [13]. The telescopic vibration of the C-H bond causes a minor vibration peak that can be observed at 2974 cm^{-1} [26]. The signal peak of Cu in Cu-CeO_2 may fall below the detection limit of FTIR owing to the low doping content of Cu.

The X-ray photoelectron spectroscopy (XPS) technique was employed to ascertain the surface element composition and electronic chemical state of Cu-CeO_2, BiOBr, and Cu-CeO_2/BiOBr. Fig. 2c shows the survey XPS spectra of Cu-CeO_2, BiOBr and 3% Cu-CeO_2/BiOBr. Cu, Ce, Bi, O and Br are present in 3% Cu-CeO_2/BiOBr samples. The regional high-resolution spectra of Cu 2p, Ce 3d, O 1s, Bi 4f and Br 3d are shown in Figs. 2d–h. In Fig. 2d, it can be observed that the peaks of Cu-CeO_2 at 932.16 eV and 935.62 eV correspond to Cu^+ and Cu^{2+} of Cu $2p_{3/2}$ respectively, while the peaks of Cu-CeO_2 at 951.94 eV and 955.91 eV are Cu^+ and Cu^{2+} of Cu $2p_{1/2}$ [19]. In addition, there is a wide signal peak at 942.77 eV, which can be attributed to the companion peak of Cu^{2+} [19]. This result confirms that the doping of Cu element mainly exists in the form of Cu^+ and Cu^{2+}. As shown in Fig. 2e, the Ce 3d spectrum is primarily composed of the Ce $3d_{3/2}$ and Ce $3d_{5/2}$ spin orbitals. The Ce $3d_{3/2}$ peak is identified as one of the three characteristic peaks of u, u", and u"', while the Ce $3d_{5/2}$ peak is identified as one of the three characteristic peaks of v, v", and v"'. These six peaks belong to the characteristic peaks of Ce^{4+}, while u' and v' indicate the existence of Ce^{3+} [30]. The XPS high-resolution spectrum of O 1s (Fig. 2f) exhibits characteristic peaks at 530.13 eV/531.48 eV and 530.05 eV/530.31 eV for Cu-CeO_2 and BiOBr, respectively. These peaks arise from lattice oxygen and hydroxyl groups on the material surface [31]. Additionally, the broad peak observed at 533.06 eV can be attributed to the presence of oxygen atoms adjacent to the oxygen vacancy in Cu-CeO_2 [32]. Fig. 2g shows the two characteristic peaks corresponding to Bi 4f in the XPS spectrum. The peaks at 159.26 eV and 164.59 eV correspond to Bi $4f_{7/2}$ and Bi $4f_{5/2}$ of BiOBr, respectively [32]. The Br 3d spectrum (Fig. 2h) reveals two distinct peaks at 68.24 eV and 69.27 eV in the BiOBr spectrum, corresponding to the electronic states of Br $3d_{5/2}$ and Br $3d_{3/2}$, respectively [31]. The high-resolution spectrum survey reveals that the Cu 2p, O 1s, Bi 4f, and Br 3d XPS spectra exhibit a marginal blue shift in the 3% Cu-CeO_2/BiOBr composite, as compared to the individual Cu-CeO_2 and BiOBr. This observation substantiates the formation of a heterojunction between the materials, leading to an augmented charge concentration [33]. Simultaneously, the maximum values of the valence band (VB) of Cu-CeO_2 and BiOBr were determined by VB-XPS, which were 2.24 eV and 2.59 eV, respectively (Fig. 2i). Combined with the subsequent UV–vis diffuse reflectance spectrum (DRS) measurement results (Fig. 3a) and the calculation formula of the minimum conduction band (CB) ($E_{CB} = E_{VB} - E_g$), the minimum conduction band values of Cu-CeO_2 and BiOBr were determined to be −0.23 eV and −0.41 eV, respectively. This finding provides a foundation for the specific mechanism analysis of photocatalytic degradation of STZ.

The degradation performance of photocatalysts is significantly influenced by the interdependent factors of light absorption and charge separation. To further corroborate the response range of the prepared samples to visible light, UV–vis DRS analysis was

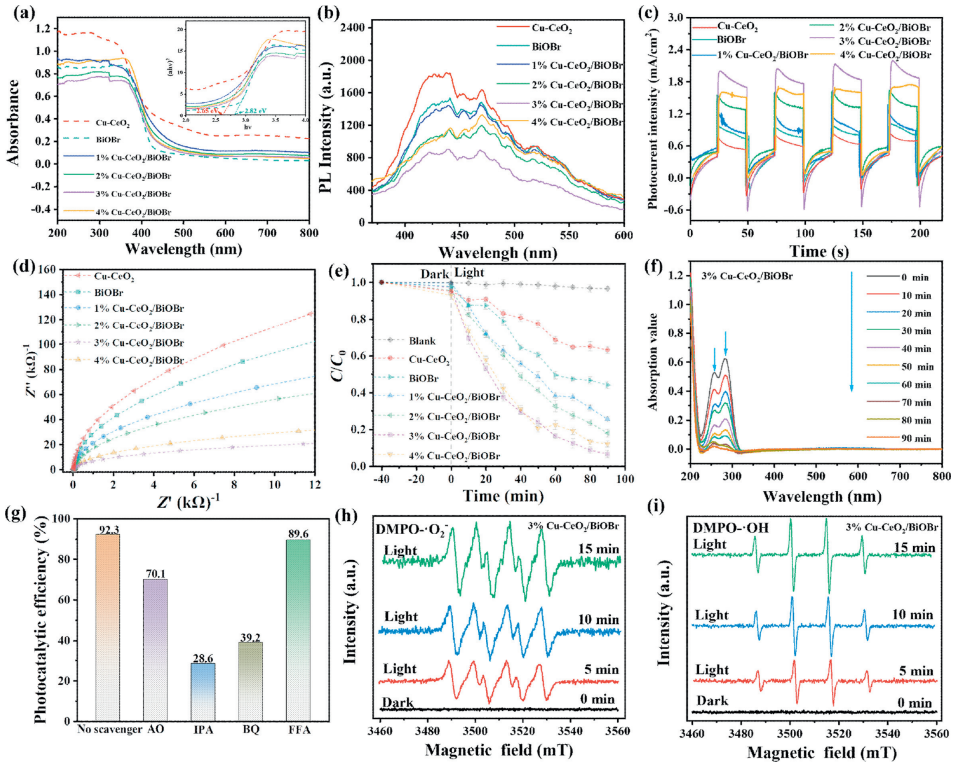

Fig. 3. (a) UV–Vis DRS of Cu-CeO_2, BiOBr and Cu-CeO_2/BiOBr (Inset is the corresponding Tauc plot). (b) Photoluminescence spectra. (c) Photodegradation efficiency of Cu-CeO_2/BiOBr. (d) Photocurrent response curves and (e) EIS spectra of Cu-CeO_2, BiOBr and Cu-CeO_2/BiOBr. (f) The variation of 3% Cu-CeO_2/BiOBr absorption with illumination time. (g) Active species trapping experiments of 3% Cu-CeO_2/BiOBr for STZ photodegradation. (h) DMPO-$^{\cdot}O_2^-$. (i) DMPO-$^{\cdot}$OH of 3% Cu-CeO_2 /BiOBr.

conducted. The data presented in Fig. 3a demonstrates that the absorption edge of Cu-CeO_2/BiOBr heterojunction materials exhibited a minor red shift in comparison to single Cu-CeO_2 or BiOBr. This shift suggests an expansion in the visible light response range, thereby enhancing the efficacy of visible light utilization. Consequently, Cu-CeO_2/BiOBr heterojunction materials possess the potential to significantly enhance visible light utilization [34]. Furthermore, according to the Tauc formula, specifically $(\alpha hv)^{1/n} = A(hv - E_g)$, where α is the molar extinction coefficient, E_g is the material band gap, v is photon frequency, h is Plank's constant, A is constant coefficient, and n is determined by the optical transition type (for indirect semiconductors like BiOBr, $n = 4$) [29]. One can derive the band gap energies of Cu-CeO_2 and BiOBr as 2.65 eV and 2.82 eV, respectively. In addition, the UV–vis DRS test result of pure CeO_2 was 2.73 eV (Fig. S1 in Supporting information), indicating that the incorporation of Cu narrowed the band gap of CeO_2, thereby improving its light absorption capacity. The photoluminescence (PL) spectrum depicted in Fig. 3b was utilized to investigate the charge separation of Cu-CeO_2/BiOBr heterojunction material. The materials exhibit a discernible peak at approximately 476 nm, with the Cu-CeO_2 displaying the highest peak intensity, followed by BiOBr, 1% Cu-CeO_2/BiOBr, 2% Cu-CeO_2/BiOBr, 4% Cu-CeO_2/BiOBr, and 3% Cu-CeO_2/BiOBr, in that order. The data reveals that the 3% Cu-CeO_2/BiOBr material exhibits the least fluorescence intensity, suggesting a reduced carrier recombination rate that enhances the photocatalyst's efficacy [35]. Fig. 3c depicts the experiment on the photocurrent response cycle. The results indicate that all materials exhibit comparable photocurrent response curves under four distinct simulated lamp switching conditions. Notably, the 3% Cu-CeO_2/BiOBr material demonstrates the most favorable photocurrent response, corroborating the findings of the PL spectrum analysis and indicating a high degree of charge separation efficiency [36]. The electrochemical impedance spectroscopy (EIS) data can be utilized to investigate the charge transfer rate of the material. As depicted in Fig. 3d, it is evident that among the Cu-CeO_2/BiOBr heterojunction materials synthesized, the 3% Cu-CeO_2/BiOBr exhibits the smallest arc radius, indicating a lower interface resistance for charge transfer and superior electron transfer capability [37]. In conclusion, the significant results from the photoelectric performance tests provide compelling evidence that the close interface between Cu-CeO_2 and BiOBr can reduce the recombination of photoexcited electron-hole pairs [38]. Notably, the 3% Cu-CeO_2/BiOBr composite exhibits superior charge separation and transport capabilities, thereby promoting the enhancement of photocatalytic performance.

To assess the antibiotic elimination efficiency of catalysts prepared in different proportions, a 20 mg/L (Fig. S2 in Supporting information) STZ solution (solution pH 7 ± 0.2 (Fig. S3 in Supporting information); catalyst dosage: 15 mg/L (Fig. S4 in Supporting information)) was employed as the model system to evaluate the photocatalytic degradation in this study. Fig. 3e demonstrates that adsorption-desorption reached equilibrium within 40 min prior to the photodegradation reaction. After 90 min of simulated visible light irradiation, it was observed that the concentration of STZ remained nearly unchanged in the control group without any catalyst, whereas pristine Cu-CeO_2 and BiOBr only achieved approximately 38.6% and 51.8% STZ removal, respectively. The Cu-CeO_2/BiOBr heterojunction materials exhibit varying removal capacities, with the order of effectiveness being 1% Cu-CeO_2/BiOBr (70.2%) < 2% Cu-CeO_2/BiOBr (79.3%) < 4% Cu-CeO_2/BiOBr (86.1%) < 3% Cu-CeO_2/BiOBr (92.3%). This suggests that the 3% Cu-CeO_2/BiOBr material demonstrates superior catalytic performance. Furthermore, the absorption value of 3% Cu-CeO_2/BiOBr at 257/281 nm exhibits a time-dependent behavior, as illustrated in Fig. 3f. Over time, the peak intensity gradually diminishes, and the highest peak undergoes a slight shift, potentially attributed to the degradation of STZ molecules into smaller molecular species. In addition, due to the possible presence of anionic

interferences in urban water (Fig. S5 in Supporting information), we also conducted a Box-Behnken (Table S4 in Supporting information) analysis to determine the optimal conditions for STX removal. Among them, the concentration of Cl^- is 37.50 mg/L, NO_3^- is 12.5 mg/L, CO_3^{2-} is 135.00 mg/L and SO_4^{2-} is 15 mg/L(Tables S5 and S6 in Supporting information).

To specifically analyze the photodegradation mechanism of the Cu-CeO_2/BiOBr system. The quenching experiment of 3%Cu-CeO_2/BiOBr degradation STZ was carried out. Consequently, three different scavengers, namely ammonium oxalate (AO), isopropanol (IPA) furfuryl alcohol (FFA) and benzoquinone (BQ), were used to quench h^+, $^{\bullet}OH$, $^1O_2$ and $^{\bullet}O_2^-$, respectively (Fig. 3g). The analysis showed that in the presence of AO, IPA, and BQ, the 3% Cu-CeO_2 /BiOBr degradation rates of STZ decreased from 92.3% to 70.1%, 28.6%, 89.6% and 39.2%, respectively. Hence, it can be deduced that the degradation reaction is primarily facilitated by $^{\bullet}OH$ and $^{\bullet}O_2^-$ as the active free radicals, while h^+ and $^1O_2$ also contribute to the elimination of STZ. ESR capture experiments were conducted on 3% Cu-CeO_2/BiOBr samples, and the corresponding ESR data was recorded in Fig. 3. As shown in Figs. 3h and i, no signal peaks were found in the dark condition at the beginning. After 5 min of visible light irradiation, signal characteristic peaks of DMPO-$^{\bullet}O_2^-$ ($A_N = 14.0$ G, $A_H = 11.0$ G) and DMPO-$^{\bullet}OH$ ($A_N = A_H = 14.9$ G) were immediately displayed [39]. As the illumination time extended, the intensity of signal peaks become higher and higher, and the ratios of signal intensity of $^{\bullet}O_2^-$ and $^{\bullet}OH$ ratio was 1:1:1:1 and 1:2:2:1 [40]. These results demonstrated the generation of $^{\bullet}O_2^-$ and $^{\bullet}OH$ during the photodegradation experiment.

The above analysis reveals that the photocatalytic degradation of STZ is predominantly facilitated by free radicals. Therefore, the theoretical calculation of the Fukui index was utilized to investigate the active sites and regional selectivity of sulfathiazole molecules.

The highest occupied molecular orbital (HOMO) of the STZ molecule (Figs. 4a and b) indicates the easy escape of electrons, making it susceptible to electrophilic attack [41]. The lowest unoccupied molecular orbital (LUMO) represents the region with the ability to acquire an electron (Fig. 4c). However, this does not offer a quantitative assessment of the reactivity for each individual atom. Fig. 4d illustrates the distribution of electrostatic potential (ESP) on the van der Waals surface of the STZ molecule, where atoms with negative (or positive) ESP indicate electron-rich (or electron-deficient) regions [40]. The sulfamide group with negative ESP is considered highly susceptible to electron loss, thereby facilitating oxidation and elimination processes. Further, the considered Fukui index is used to quantitatively describe the reaction reactivity of each atom (Fig. 4e). The primary ROS in this reaction system, $^{\bullet}OH$ is widely considered as an electrophilic radical, while $^{\bullet}O_2^-$ is considered as a weak nucleophilic radical [42,43]. The results indicate that the N1 ($f^- = 0.082$), C3 ($f^- = 0.062$), C11 ($f^- = 0.139$) and S12 ($f^- = 0.088$) atoms with the highest electrophilic attack Fukui indexes are the most reactive sites inclined to be attacked by $^{\bullet}OH$. Besides, the N1 ($f^0 = 0.075$), C2 ($f^0 = 0.061$), C5 ($f^0 = 0.063$), C11 ($f^0 = 0.079$) and S12 ($f^0 = 0.112$) atoms with the highest radical attack Fukui indexes are the most reactive sites inclined to be attacked by $^{\bullet}O_2^-$. Moreover, $^{\bullet}O_2^-$ also can be considered as a weak nucleophilic radical, then the Fukui index for nucleophilic attack (f^+) is further explored. The C2 ($f^+ = 0.088$), C5 ($f^+ = 0.075$), S12 ($f^+ = 0.136$), O14 ($f^+ = 0.068$) and C15 ($f^+ = 0.067$) atoms with the highest f^+ values are the most reactive sites for nucleophilic attack. In comparison, $^{\bullet}O_2^-$ is superior in attacking S site in the thiazolyl group, as a weak nucleophilic specie, especially the S12 site. While $^{\bullet}OH$ prefer to attack the C site in the thiazolyl group and N site in the terminal amino group.

LC-MS analysis was conducted to detect the degradation intermediates of STZ, and their retention time and *m/z* values are presented in Table S6. The photocatalytic degradation of STZ primarily occurs through mechanisms involving chemical bond breaking, oxidation, and substitution [44]. Fig. 4f illustrates the potential degradation pathway of STZ to 3% Cu-CeO_2/BiOBr under xenon lamp irradiation, in conjunction with theoretical calculations. The initial step involves the cleavage of a chemical bond, resulting in the formation of P1 ($m/z = 173$) from the C-N bond cleavage and P2 ($m/z = 93$) from the S-C bond breaking, leading to the generation of P3 ($m/z = 125$) [45,46]. This is consistent with the DFT results. In the subsequent stage, the thiazole ring is attacked by $^{\bullet}OH$ resulting in the production of SO_4^{2-} and short chains of organic acids, giving rise to P4 ($m/z = 216$). P4 undergoes persistent oxidation, resulting in the formation of xanthamide P1 ($m/z = 173$) through the dissociation of the N-C=O bond. Ultimately, the oxidative degradation of these compounds culminates in the disintegration of the aromatic ring, concomitant with the generation of H_2O, CO_2, and inorganic salt ions, including NH_4^+, NO_3^-, and SO_4^{2-} [47]. To further understand the degradation performance of the 3% Cu-CeO_2/BiOBr system, we measured the residual total organic carbon (TOC) content in the 3% Cu-CeO_2/BiOBr system. As shown in Fig. S6 in Supporting information, the 3% Cu-CeO_2/BiOBr system achieves a TOC removal efficiency of about 49%.

Based on the above analysis results, we proposed the potential mechanism of 3% Cu-CeO_2/BiOBr photocatalytic enhancement, as shown in Fig. 5. Under light conditions, both Cu-CeO_2 and BiOBr can be excited by light to produce e^- and h^+ substances. In general, e^- tends to migrate to positions where the potential is corrected, and h^+ tends to migrate to positions where the potential is more negative. However, the conduction position of BiOBr (−0.23 eV) was more correct than that of $O_2/^{\bullet}O_2^-$ (−0.33 eV), and the valence band position of Cu-CeO_2 (2.24 eV) was more negative than that of $H_2O/^{\bullet}OH$ (2.38 eV), which could not produce active free radicals $^{\bullet}O_2^-$ and $^{\bullet}OH$ that degraded STZ. This contradicts our degradation efficiency and ESR results [48]. There-

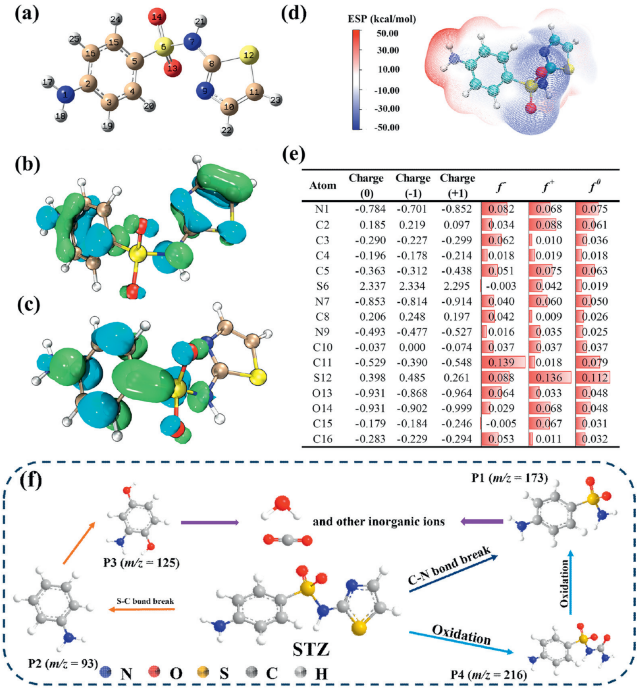

Atom	Charge (0)	Charge (-1)	Charge (+1)	f^-	f^+	f^0
N1	-0.784	-0.701	-0.852	0.082	0.068	0.075
C2	0.185	0.219	0.097	0.034	0.088	0.061
C3	-0.290	-0.227	-0.299	0.062	0.010	0.036
C4	-0.196	-0.178	-0.214	0.018	0.019	0.018
C5	-0.363	-0.312	-0.438	0.051	0.075	0.063
S6	2.337	2.334	2.295	-0.003	0.042	0.019
N7	-0.853	-0.814	-0.914	0.040	0.060	0.050
C8	0.206	0.248	0.197	0.042	0.009	0.026
N9	-0.493	-0.477	-0.527	0.016	0.035	0.025
C10	-0.037	0.000	-0.074	0.037	0.037	0.037
C11	-0.529	-0.390	-0.548	0.139	0.018	0.079
S12	0.398	0.485	0.261	0.088	0.136	0.112
O13	-0.931	-0.868	-0.964	0.064	0.033	0.048
O14	-0.931	-0.902	-0.999	0.029	0.068	0.048
C15	-0.179	-0.184	-0.246	-0.005	0.067	0.031
C16	-0.283	-0.229	-0.294	0.053	0.011	0.032

Fig. 4. (a) Chemical structure, (b) highest occupied molecular orbital (HOMO), (c) lowest unoccupied molecular orbital (LUMO), and (d) electrostatic potential (ESP) distribution of STZ. (e) Natural population analysis (NPA) charge distributions and condensed Fukui index (f^-, f^+ and f^0) of STZ. (f) The proposed STZ degradation pathway.

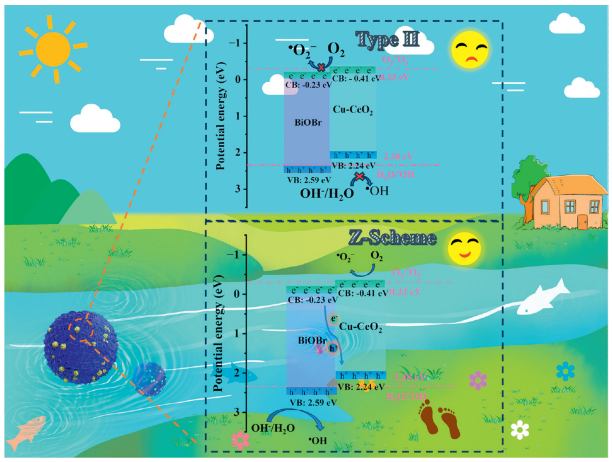

Fig. 5. Possible mechanism of photocatalytic degradation of 3% Cu-CeO_2/BiOBr.

fore, Z-type heterojunction is more suitable for the photocatalytic degradation mechanism of 3% Cu-CeO_2/BiOBr photocatalyst, that is, electrons in BiOBr conduction band and h^+ in Cu-CeO_2 valence band to form an internal electric field, so that h^+ and e^- are retained in the conduction band of Cu-CeO_2 and the valence band of BiOBr, respectively. Thus, the recombination of photogenerated e^- and h^+ is inhibited. Because the conduction position of Cu-CeO_2 (−0.41 eV) is more negative than that of $O_2/{}^{\bullet}O_2^-$ (−0.33 eV), the valence band position of BiOBr (2.59 eV) is more correct than that of $H_2O/{}^{\bullet}OH$ (2.38 eV). Consequently, 3% Cu-CeO_2/BiOBr has a high redox potential, which can simultaneously produce active substances such as ${}^{\bullet}O_2^-$, ${}^{\bullet}OH$ and h^+ [49]. Ultimately, these active radicals with strong oxidation–reduction ability decompose STZ molecules into CO_2, H_2O and some harmless inorganic substances.

To summarize, Cu-CeO_2/BiOBr Z-type heterojunction photocatalyst can be directly synthesized by calcination and solvothermal method. Compared to pristine Cu-CeO_2 and BiOBr, Cu-CeO_2/BiOBr has shown significantly enhanced photocatalytic degradation performance towards sulfathiazole under visible light irradiation. Notably, 3% Cu-CeO_2/BiOBr exhibits the greatest photocatalytic activity, with STZ removal exceeding 92% within 90 min of visible light irradiation. After five cycle experiments, 3% CuO_2/BiOBr still has a high degradation rate, indicating that the material has a certain cycle stability (Fig. S7 in Supporting information). At the same time, the degradation rate of STZ in tap water can reach 76% (Fig. S8 in Supporting information), and it also has a good effect in actual water bodies. This is primarily due to the formation of a heterojunction between Cu-CeO_2 and BiOBr, which boosts charge transfer and separation. Moreover, the presence of Cu-CeO_2 greatly adjusts the energy band structure, enhances the visible light absorption capability of Cu-CeO_2/BiOBr, and generates more active species. Furthermore, the experiment revealed that the photocatalyst is considerably stable and exhibits exceptional photodegradation performance even after five repeated uses. To conclude, this study not only proposes a viable photocatalytic system for eliminating STZ from environmental wastewater, but also offers a novel approach for designing distinctive heterojunction nanomaterials based on BiOBr in the future.

Declaration of competing interest

The authors declare that they have no known competing financial interests or personal relationships that could have appeared to influence the work reported in this paper.

Acknowledgment

This work was supported by the National Natural Science Foundation of China (Nos. 21471103, 52372212).

Supplementary materials

Supplementary material associated with this article can be found, in the online version, at doi:10.1016/j.cclet.2023.109245.

References

[1] Z. Gao, H. Yang, J. Mao, et al., J. Clean. Prod. 220 (2019) 668–676.
[2] N. de Melo Costa Serge, R.G.L. Gonçalves, H.D. Rojas-Mantilla, et al., J. Hazard. Mater. 413 (2021) 125388.
[3] S. Feng, M. Yu, T. Xie, et al., Chem. Eng. J. 433 (2022) 134467.
[4] D. Li, G. Zhang, W. Li, et al., J. Clean. Prod. 380 (2022) 135064.
[5] S. Yang, D. Tian, X. Wang, et al., Sep. Purif. Technol. 308 (2023) 122900.
[6] L. Zhu, Q. Yan, M. Ran, et al., Chin. Sci. Bull. 68 (2023) 892–896.
[7] D. Vaya, P.K. Surolia, Environ. Technol. Innov. 20 (2020) 101128.
[8] C. Deng, T. Wang, F. Ye, et al., J. Environ. Chem. Eng. 10 (2022) 107365.
[9] V. Subhiksha, S. Kokilavani, S. Sudheer Khan, Chemosphere 290 (2022) 133228.
[10] J. Niu, K. Wang, L. Yang, et al., Opt. Mater. 134 (2022) 113125.
[11] J. Xie, X. Zhang, Z.J. Lu, et al., Inorg. Chem. Front. 10 (2023) 5127–5135.
[12] B. Liu, X. Hu, J. Yang, et al., Catal. Sci. Technol. 13 (2023) 504–515.
[13] F. Guo, J. Chen, J. Zhao, et al., Chem. Eng. J. 386 (2020) 124014.
[14] R. Ma, S. Zhang, T. Wen, et al., Catal. Today 335 (2019) 20–30.
[15] H. Wu, Q. Sun, J. Chen, et al., Chem. Eng. J. 425 (2021) 130640.
[16] S. He, C. Yan, X.Z. Chen, et al., Appl. Catal. B: Environ. 276 (2020) 119138.
[17] M. Shi, B. Rhimi, K. Zhang, et al., Chemosphere 275 (2021) 130083.
[18] S.M. Chaudhari, O.S. Gonsalves, P.R. Nemade, Mater. Res. Bull. 143 (2021) 111463.
[19] M. Mousavi Kamazani, F. Azizi, Ultrason. Sonochem. 58 (2019) 104695.
[20] Y. Mei, Y. Zhang, J. Li, et al., J. Alloys Compd. 904 (2022) 163879.
[21] A. Shahzadi, S. Moeen, A.D. Khan, et al., ACS Omega 8 (2023) 8605–8616.
[22] G.Pedroza Herrera, I.E. Medina Ramírez, J.A. Lozano Álvarez, et al., Catal. Today 341 (2020) 37–48.
[23] B. Xiao, M. Xu, B. Lu, et al., J. Phys. Chem. Solids 163 (2022) 110583.
[24] F. Hayati, M.R. Khodabakhshi, A.A. Isari, et al., J. Water Process Eng. 38 (2020) 101693.
[25] X.J. Wen, C. Zhang, C.G. Niu, et al., Catal. Commun. 90 (2017) 51–55.
[26] T. Jia, J. Wu, Y. Xiao, et al., J. Colloid Interface Sci. 587 (2021) 402–416.
[27] F. Du, Z. Lai, H. Tang, et al., Chemosphere 287 (2022) 132391.
[28] S.E. George, M. George, J. Alex, et al., Ceram. Int. 46 (2020) 13932–13940.
[29] Y. Wu, H. Ji, Q. Liu, et al., J. Hazard. Mater. 424 (2022) 127563.
[30] Y. Zhang, M. Wu, Y. Wang, et al., J. Mater. Sci. Technol. 116 (2022) 169–179.
[31] D. Liu, D. Chen, N. Li, et al., Angew. Chem. Int. Ed. 59 (2020) 4519–4524.
[32] Y. Ou, J. Shi, Q. Yan, et al., Inorg. Chem. Commun. 133 (2021) 108867.
[33] H. Liu, W. Huo, T.C. Zhang, et al., Mater. Today Chem. 23 (2022) 100729.
[34] W. Zhou, B. Yang, G. Liu, et al., J. Colloid Interface Sci. 615 (2022) 849–864.
[35] Z. Liu, J. Tian, C. Yu, et al., Chin. J. Catal. 43 (2022) 472–484.
[36] K. Liu, H. Zhang, Y. Muhammad, et al., Sep. Purif. Technol. 274 (2021) 118992.
[37] Z. He, M.S. Siddique, H. Yang, et al., J. Clean. Prod. 339 (2022) 130634.
[38] S. Huang, F. Feng, R.T. Huang, et al., Adv. Mater. 34 (2022) 2208438.
[39] L. Chen, J. Duan, P. Du, et al., Water Res. 221 (2022) 118747.
[40] J. Qi, X. Yang, P.Y. Pan, et al., Environ. Sci. Technol. 56 (2022) 5200–5212.
[41] M. Li, Q. Mei, D. Han, et al., Sci. Total Environ. 768 (2021) 144733.
[42] H. Zhang, C. Xie, L. Chen, et al., Water Res. 229 (2023) 119392.
[43] M. Zhang, J. He, Y. Chen, et al., Chin. Chem. Lett. 31 (2020) 2721–2724.
[44] Z. Hu, X. Xie, S. Li, et al., Chem. Eng. J. 404 (2021) 126541.
[45] Z. Cai, Y. Huang, H. Ji, et al., Sep. Purif. Technol. 280 (2022) 119772.
[46] F. Deng, S. Qiu, H. Olvera Vargas, et al., Electrochim. Acta 297 (2019) 21–30.
[47] X. Sun, L. Shi, Q. Bai, et al., Appl. Surf. Sci. 587 (2022) 152633.
[48] X. Hua, H. Chen, C. Rong, et al., J. Hazard. Mater. 448 (2023) 130951.
[49] Y. Xue, Z. Chen, Z. Wu, et al., Sep. Purif. Technol. 275 (2021) 119152.